Orbital-free density functional theory simulation of collective dynamics coupling in liquid Sn

Beatriz G. del Rio, Mohan Chen, Luis E. González, and Emily A. Carter

Citation: The Journal of Chemical Physics **149**, 094504 (2018); doi: 10.1063/1.5040697
View online: https://doi.org/10.1063/1.5040697
View Table of Contents: http://aip.scitation.org/toc/jcp/149/9
Published by the American Institute of Physics

Orbital-free density functional theory simulation of collective dynamics coupling in liquid Sn

Beatriz G. del Rio,[1,2] Mohan Chen,[3] Luis E. González,[1] and Emily A. Carter[4,a)]
[1]*Departamento de Física Teórica, Atómica y Óptica, Universidad de Valladolid, 47011 Valladolid, Spain*
[2]*Department of Mechanical and Aerospace Engineering, Princeton University, Princeton, New Jersey 08544-5263, USA*
[3]*Department of Physics, Temple University, Philadelphia, Pennsylvania 19122, USA*
[4]*School of Engineering and Applied Science, Princeton University, Princeton, New Jersey 08544-5263, USA*

(Received 19 May 2018; accepted 19 July 2018; published online 6 September 2018)

The appearance of a second excitation mode in the longitudinal and transverse collective dynamics of a series of liquid metals has been observed recently, either by inelastic X-ray scattering (IXS) or by first-principles molecular dynamics (FPMD). The phenomenon's origin is still uncertain, although some theories have been used with relative success to reproduce the FPMD results as a means to find an explanation for it (e.g., mode-coupling (MC) theory in liquid zinc [B. G. del Rio and L. E. González, Phys. Rev. B **95**, 224201 (2017)]). For liquid tin (*l*-Sn), the second excitation mode in the dynamic structure factor and longitudinal current spectrum was observed by IXS [S. Hosokawa *et al.*, J. Phys.: Condens. Matter **25**, 112101 (2013)]. By performing orbital-free density functional theory MD simulations of *l*-Sn, we confirm the existence of a second excitation mode in the longitudinal and transverse collective dynamics and provide a theoretical explanation based on MC theory. Moreover, we introduce a new binary term in MC theory to better capture the negative minima present in the memory functions of the collective dynamics. These results confirm that the origin of the second excitation mode exhibited by the longitudinal and transverse collective dynamics in some liquid metals involves an indirect coupling of the longitudinal and transverse modes. *Published by AIP Publishing.* https://doi.org/10.1063/1.5040697

I. INTRODUCTION

One of the main research areas in liquid theory is the collective-dynamics behavior of non-simple liquid metals. Two different limits of such behavior are well understood: the hydrodynamic regime and free-particle regime.[1,2] In the hydrodynamic regime [wave vectors (q) → 0, time (t) → ∞], the liquid behaves like a continuum and is characterized by the macroscopic conservation laws of mass, momentum, and energy. As a result, the main mechanisms governing longitudinal dynamics behavior are thermal relaxation and the propagation of collective waves, also known as propagating modes. However, the propagation of collective waves does not occur for transverse dynamics; they instead decay in time due to the presence of shear viscosity. By contrast, in the free particle regime (q → ∞, t → 0), both the longitudinal and transverse dynamics are dominated by the thermal velocity of the particles, and the propagation of collective waves is not supported in either direction.

Intermediate between the hydrodynamic and free-particle regimes is the kinetic regime, which is the least understood and therefore has attracted most of the recent research in liquid metals.[3–9] The kinetic regime is controlled by additional mechanisms that increase the complexity of both the longitudinal and transverse dynamics. For example, viscoelasticity appears in the transverse dynamics, causing the propagation of shear waves, while it leads to the phenomenon of "positive dispersion" in the longitudinal dynamics, which increases the phase velocity at small wave vectors with respect to the hydrodynamic speed of sound.[10]

Many theoretical models have been developed or extended from the hydrodynamic regime to the kinetic regime, in order to provide insight into the governing mechanisms underlying the complex collective dynamics of non-simple liquid metals. For example, the generalized hydrodynamic model extends the hydrodynamic regime model by allowing the variables to depend on the wave vector.[11] Mode-coupling (MC) theories, originally developed to study the relaxation behavior of the liquid-glass transition, also have been modified to consider liquid metals.[12]

Third-generation synchrotron facilities, along with the ability to energetically discriminate X-rays with high resolution, have made inelastic X-ray scattering (IXS) a reliable method to study collective dynamics in disordered systems.[13–16] Experiments have uncovered complex collective-dynamics behavior as a result. One such complex behavior observed in IXS experiments is the appearance of a second mode in the longitudinal collective dynamics in several

a)Author to whom correspondence should be addressed: eac@princeton.edu

non-simple liquid metals. The first experiments demonstrating the existence of this second mode at small frequencies were carried out by Hosokawa *et al.*[17] on liquid gallium (*l*-Ga). Since then, measurements on other liquid metals, such as tin (Sn), iron (Fe), zinc (Zn), and copper (Cu),[18,19] exhibited this feature, as well. In all of these experiments, only wave vectors lower than half of the position of the main peak, q_p, in the static structure factor, S(q), were sampled. Hosokawa *et al.* related the appearance of the second mode to a direct coupling of the transverse collective dynamics with the longitudinal collective dynamics.

Subsequent first-principles molecular dynamics (MD) calculations performed on *l*-lithium (Li),[20] *l*-Fe,[21] and *l*-sodium (Na)[22] at high pressures also revealed the existence of a second mode in the transverse dynamics. This second mode was visible in the wave-vector region around q_p at frequencies higher than the main transverse mode and was thought to be unique to high-pressure dynamics. However, recent simulations observed the presence of this second mode in the transverse dynamics of *l*-Ni[23] and *l*-Zn,[24] both at zero pressure. All of these results point to a complex feature for which a full understanding is lacking. For example, Kohn-Sham density functional theory molecular dynamics (KSDFT-MD) simulations by Bryk *et al.*[20] of *l*-Li at 1000 K and pressures ranging from 1 atm up to 186 GPa found a second mode in both the longitudinal and transverse dynamics emerged at 125 GPa and became more pronounced as pressure increased. Bryk *et al.* applied a thermo-viscoelastic model to the longitudinal dynamics and an extended viscoelastic model to the transverse dynamics; both are five-variable-based models, although each of them used different dynamical variables. Bryk *et al.* were able to explain the appearance of this second mode in both the longitudinal and the transverse dynamics using these models. However, the models failed to provide an explanation for possible cross-correlations between the longitudinal and transverse modes. Employing a different theoretical formalism, two of us recently applied MC theory to study *l*-Zn at 0 GPa with KSDFT-MD.[24] The MC approach also reproduces the second mode in both the longitudinal and transverse dynamics; however, we attributed the existence of the second mode to a coupling between the longitudinal and transverse collective dynamics. In addition, we related the frequency of the second mode in the transverse dynamics to the frequencies of the longitudinal dynamics.

In the present work, we provide a theoretical explanation for the existence of and connection between modes in the collective dynamics of *l*-Sn. Notably, the atomic structure of *l*-Sn differs greatly from *l*-Zn: *l*-Sn is an open system where most atoms have four nearest neighbors, whereas *l*-Zn is closest-packed where atoms are surrounded by 12 nearest neighbors. By comparing the dynamics of *l*-Sn to those of *l*-Zn, we test further the hypothesis that MC is responsible for the second mode in the collective dynamics. A previous KSDFT-MD simulation of 205 atoms of *l*-Sn by Calderín *et al.*[6] did not observe a second mode in the collective dynamics, although other calculated properties compared well with experiment. A plausible reason could be the need to model a larger number of atoms to correctly represent this phenomenon in *l*-Sn. Therefore, in this study, we performed orbital-free density functional theory molecular dynamics (OFDFT-MD)[25–28] simulations, which enable investigation of systems containing thousands of atoms and facilitate a detailed study of the collective dynamics with high accuracy due to much better statistics. The OFDFT-MD simulations were conducted at 0 GPa and 573 K, near the melting point. We observe a second mode in the longitudinal collective dynamics from the simulation results, at either lower or higher frequencies than the main mode. Moreover, a high-frequency second mode in the transverse collective dynamics also appears. To provide theoretical insight into these features, we use the same theoretical approach applied in our previous study of *l*-Zn,[24] based on MC theory.[2,29–32] Overall, the theory correctly reproduces both the longitudinal and transverse collective dynamics of *l*-Sn. MC also explains the appearance of this second mode as a consequence of indirect coupling between the longitudinal and transverse collective dynamics.

The layout of the paper is as follows. In Sec. II, we describe the details of the OFDFT-MD simulations of *l*-Sn and give the theoretical expressions and formulations used to evaluate physical properties. In Sec. III, we first compare the accuracy of our simulation results with previous computational and experimental data. We next evaluate the collective dynamics of *l*-Sn directly from OFDFT-MD and identify the second mode present in both the longitudinal and transverse collective dynamics. We then provide an explanation for the appearance and behavior of the second mode in the collective dynamics by using different formulations of MC theory. Finally, an assessment of the overall success of MC theory, along with guidelines for future theoretical improvements, is presented in Sec. IV.

II. METHODOLOGY

A. Computational details

The total energy of N classical ions each with charge Z, located at positions $\vec{R}_i$ in a volume V and interacting with $N_e = NZ$ valence electrons, may be written within the Born-Oppenheimer approximation as the sum of the ion kinetic energy, the direct Coulomb interaction energy between the ions, and the ground-state energy of the electrons in the presence of the ions. The last term can be evaluated accurately within DFT. In general, the orbital-based KSDFT[33] can be used to perform calculations for up to hundreds of atoms. However, with a computational cost increasing cubically with the system size for conventional implementations, KSDFT is an expensive tool for systems with thousands of atoms. A better choice for these large systems is the density-based OFDFT,[25–28] which easily treats thousands of atoms due to its quasi-linear scaling, $O(N \log N)$. However, state-of-the-art implementations of OFDFT tend to fail for systems with strongly varying electron densities, and additional efforts therefore are required to validate its accuracy first.

The OFDFT energy functional is expressed as

$$E[n(\vec{r})] = T_s[n(\vec{r})] + E_{ext}[n(\vec{r})] + E_H[n(\vec{r})] + E_{xc}[n(\vec{r})], \quad (1)$$

where T_s represents the kinetic energy of a non-interacting electronic system with electron density $n(\vec{r})$,[26] E_{ext} typically is the electron-ion interaction energy due to the potential created by the ions,

$$E_{ext}[n(\vec{r})] = \int n(\vec{r})V_{ext}(\vec{r})d\vec{r}. \quad (2)$$

E_H is the Hartree term due to the electrostatic repulsion between the electrons,

$$E_H[n(\vec{r})] = \frac{1}{2}\int\int \frac{n(\vec{r})n(\vec{s})}{|\vec{r}-\vec{s}|}d\vec{r}d\vec{s}, \quad (3)$$

and E_{xc} is the electron exchange-correlation (XC) energy.

In our simulations, the E_{ext} term is modelled using a local pseudopotential (LPS), which represents the effect of the screened ion (nucleus plus core electrons) on the valence electron density, $n(\vec{r})$. Here, the bulk-derived local pseudopotential (BLPS) algorithm was used to construct it.[34,35] This method emphasizes reproducing the crystalline properties obtained from KSDFT results and does not guarantee a correct representation of the liquid state. Although *l*-Li was studied with OFDFT using a BLPS, providing an accurate melting point and diffusion coefficients,[36] such calculations on *l*-Sn using a BLPS were found to be insufficiently accurate (see Sec. S1 of the supplementary material). These shortcomings arising from the BLPS can be overcome by a recently developed force-matching (FM) method.[9] The main idea of the FM method is to add functional flexibility to a chosen LPS so as to minimize the differences between KSDFT and OFDFT forces on atoms in a given liquid configuration. Details of the BLPS algorithm, KSDFT benchmark calculations, BLPS construction, and final LPS obtained through the FM method are provided in Sec. S1 of the supplementary material.

Periodic OFDFT calculations were performed with the PROFESS (PRinceton Orbital-Free Electronic Structure Software) code developed by the Carter group.[37–39] We found a reasonable performance of the LPS for a variety of physical properties of *l*-Sn when paired with the Smargiassi-Madden (SM) kinetic energy density functional (KEDF)[40] and the local density approximation (LDA) XC functional,[41] as parametrized by Perdew and Zunger (*vide infra* and Sec. S2 of the supplementary material).[42] The kinetic energy cutoff was set to 1200 eV to ensure that the accuracy of the total energy is converged to within 1.0 meV/atom. The atomic densities of *l*-Sn at different temperatures were obtained by performing MD simulations with the isothermal-isobaric (NPT) ensemble and the Parrinello-Rahman barostat[43] on systems of 512 atoms for a total time of 30 ps with a time step of 0.5 fs. A thermostat mass of 5×10^4 a.u. was used along with a barostat mass of 10^9 a.u. in order to minimize the oscillations and drift in the temperature and pressure of the system. Once the atomic densities were determined (Table S.I in the supplementary material), we studied *l*-Sn at each temperature by first thermalizing a system of 1000 atoms for a total of 6 ps, using a time step of 4 fs within the NVT ensemble with a Nosé-Hoover thermostat mass of 10^5 a.u.[44,45] After the systems reached the energy equilibrium, we performed NVE simulations at each temperature using 1000 atoms with a time step of 4 fs (sufficiently short to conserve energy) for a total time of 80 ps to gather final statistics for the properties reported herein.

B. Liquid metal theory

One basic dynamical variable used to characterize the thermal movement of atoms in a liquid is the q-dependent atomic density defined as $\rho(\vec{q},t) = \sum_{i=1}^{N}\exp(-i\vec{q}\cdot\vec{r}_i(t))$, where $\vec{r}_i(t)$ is the position of the i-th atom at time t.[1,2] The intermediate scattering function F(q, t) is defined as the time-autocorrelation function of this quantity,

$$F(q,t) = \frac{1}{N}\langle\rho(\vec{q},t+t_0)\rho(-\vec{q},t_0)\rangle, \quad (4)$$

where averages are taken over wave vectors and time origins. Details on the time origins and the number of time steps used in the correlations for every wave-vector region are given in Sec. S3 of the supplementary material.

Some of the most interesting phenomena to study in liquid-state dynamics are the existence of propagating modes in the system. These propagating modes represent collective density fluctuations traveling in a manner that is analogous to a phonon in a solid. The Fourier Transform (FT) of F(q, t) into the frequency domain yields the dynamic structure factor $S(q,\omega)$; a maximum in $S(q,\omega)$ at $\omega \neq 0$ is proof of the existence of propagating modes in the liquid. However, these maxima are difficult to observe experimentally, and their calculation from MD trajectories can also be challenging. In fact, there is not yet a theory for correctly describing the behavior of these modes outside the hydrodynamic regime ($q \to 0$). It therefore is impossible to know beforehand whether or not a system can support these propagating modes and, if so, in which wavelength and frequency range.

The scattered intensity obtained in an IXS experiment is directly related to $S(q,\omega)$; however, a proper comparison of the OFDFT-MD results and IXS data must account for the difference between the simulations and actual phonon scattering, as the former treats the ions classically while the latter is a quantum process.[46] Therefore, to properly compare to the IXS measurements, the $S(q,\omega)$ obtained from OFDFT-MD is corrected to fulfill the detailed balance condition,[3,47]

$$S_Q(q,\omega) = \frac{\hbar\beta\omega}{1-e^{-\hbar\beta\omega}}S(q,\omega), \quad (5)$$

where $\beta = \frac{1}{k_B T}$ with the Boltzmann constant k_B and the temperature T. Moreover, the experimental setup is characterized by an energy resolution, which is accounted for in our simulation results through the convolution of $S_Q(q,\omega)$ with the experimental resolution function $R(\omega)$,

$$I(q,\omega) = E(q)\int d\omega' S_Q(q,\omega')R(\omega-\omega'), \quad (6)$$

where E(q) is a normalization factor including the effect of the scattering geometries and the experimental setup. In the

IXS experiments performed by Hosokawa *et al.*[18] for *l*-Sn, the experimental resolution factor takes the following form:

$$R(\omega) = \frac{c}{\pi(\omega^2 + c^2)}, \tag{7}$$

with $c = \frac{\Delta E}{2}$, where $\Delta E = 2.28\ ps^{-1}$ is the energy resolution in the experiment. The normalization factor E(q) is introduced to rescale the experimental data (reported in arbitrary units) for the final comparison between the OFDFT-MD and IXS data. The rescaling is chosen such that the height of the side peaks in both cases is similar.

Another important dynamical variable is the atom velocity. The correlation function of the atom velocity, known as the velocity autocorrelation function (VACF), Z(t), provides atom diffusion information and is defined as

$$Z(t) = \frac{\langle \vec{v}_i(t + t_0) \cdot \vec{v}_i(t_0) \rangle}{\langle \vec{v}_i(t_0) \cdot \vec{v}_i(t_0) \rangle}, \tag{8}$$

where $\vec{v}_i(t)$ is the velocity of the i-th atom. Z(t) is a measure of the projection of the atom velocity at time t onto its initial value at time t_0, averaged over all initial values. In this study, correlations were performed over sets of 500 time steps by taking time origins at each time step. The FT of Z(t) is the power spectrum, $Z(\omega)$, providing information about the main characteristic frequencies of the system, e.g., the main vibrational modes or possible coupling between the atoms' velocities and currents, as defined next.

The collective motion of the atoms in a liquid metal is studied via the atom current, $\vec{J}(\vec{r}, t)$,

$$\vec{J}(\vec{r}, t) = \sum_{i=1}^{N} \vec{v}_i(t)\delta(\vec{r} - \vec{R}_i(t)), \tag{9}$$

where $\vec{v}_i$ is the velocity of the i-th atom. By performing a FT of $\vec{J}(\vec{r}, t)$, we obtain

$$\vec{J}(\vec{q}, t) = \sum_{j=1}^{N} \vec{v}_j(t) e^{-i\vec{q}\cdot\vec{R}_j(t)}, \tag{10}$$

which can be split into the longitudinal and transverse components of the wave vector $\vec{q}$, $\vec{J}_T(\vec{q}, t)$ and $\vec{J}_L(\vec{q}, t)$, respectively. The longitudinal and transverse autocorrelation functions are defined as the autocorrelation functions of the respective components of the current,

$$C_L(q, t) = \frac{1}{N}\langle \vec{J}_L(\vec{q}, t) \cdot \vec{J}_L(-\vec{q}, 0) \rangle, \tag{11}$$

$$C_T(q, t) = \frac{1}{2N}\langle \vec{J}_T(\vec{q}, t) \cdot \vec{J}_T(-\vec{q}, 0) \rangle. \tag{12}$$

Details on the time origins and the number of time steps used in the correlations for every wave-vector region are given in Sec. S3 of the supplementary material. The longitudinal current correlation function is directly related to the intermediate scattering function via

$$C_L(q, t) = -\frac{1}{q^2}\frac{\partial^2 F(q, t)}{\partial t^2}. \tag{13}$$

From this relation, it can be deduced that both correlation functions, $C_L(q, t)$ and $F(q, t)$, in essence contain the same information.

The FTs of $C_L(q, t)$ and $C_T(q, t)$ into the frequency domain are defined as $C_L(q, \omega)$ and $C_T(q, \omega)$, respectively. Both $C_L(q, \omega)$ and $C_T(q, \omega)$ can exhibit propagating modes; however, while $C_L(q, \omega)$ supports propagating modes in the hydrodynamic regime, $C_T(q, \omega)$ does not. It is well established that liquids, from a microscopic point of view, cannot support shear waves as solids do.[2] Accordingly, transverse current fluctuations in the hydrodynamic regime decay through diffusive modes. However, in the kinetic regime, where deformations in the wavelength and frequencies at the microscopic scale are considered, $C_T(q, \omega)$ can exhibit maxima at $\omega \neq 0$.

C. Fitting model

Propagating modes in $S(q, \omega)$, $C_L(q, \omega)$, and $C_T(q, \omega)$ do not always appear as peaks. Sometimes, these modes appear as shoulders, making the study of the complete dispersion relation a challenging process where it is necessary to fit the functions to a model. When Hosokawa *et al.*[17] first observed the second propagating mode in $C_L(q, t)$, they fit both $C_L(q, t)$ and $C_T(q, t)$ to a model composed of two Gaussians. However, this fitting model had at least two shortcomings: no diffusive mode contribution was included and the expressions violated the basic physical properties of the collective dynamic functions.

We instead employ a fitting model previously introduced in the study of *l*-Zn.[24] This model is composed of a hyperbolic secant for the diffusive term and a modified damped harmonic oscillator (MDHO) for the propagating mode,

$$f^{diff}(t) = \alpha \mathrm{sech}(\beta t), \tag{14}$$

$$f^{MDHO}(t) = A\left(\frac{\cos(\Omega t)}{\cosh(\gamma t)} + \frac{\gamma}{\Omega}\frac{\sin(\Omega t)}{\sinh(\gamma t)}\right). \tag{15}$$

Within this model, both $F(q, t)$ and $C_T(q, t)$ are directly fitted to one diffusive term [Eq. (14)] and one or two MDHOs [Eq. (15)]. Given the relationship between $C_L(q, t)$ and $F(q, t)$ [Eq. (13)], the longitudinal current correlation functions were fitted to the second derivative of the model used for $F(q, t)$. Both $F(q, t)$ and $C_L(q, t)$ were fitted jointly using the same values for all of the parameters. In contrast with Hosokawa *et al.*'s model, this model complies with the conditions of exponential decay at long times and time-reversal symmetry, leading to free-particle-like behavior for short times.

The dispersion relation for each mode is obtained from the position in frequency of the maximum of each MDHO, which we denote as Ω_L and Ω_T. The longitudinal mode natural frequencies, Ω_L, are given by the maxima in $\omega^2 S(q, \omega)$. The position in the frequency of the maximum of each mode from MD will be represented by ω_m for $S(q, \omega)$, ω_L for $C_L(q, \omega)$, and ω_T for $C_T(q, \omega)$.

D. Mode coupling

The behavior of the memory functions (see the Appendix for further details) of a given dynamical variable is ruled by

several rates of decay, but only the slowest of them survives for long times. The main idea behind MC is to consider this long-lasting term as a coupling of the studied variable with other slowly decaying variables, known as modes.[2] Since the 1970s, different MC formalisms have been developed to study the correlation functions of several variables and functions, such as the particle velocity (i.e., VACF),[48,49] particle density (F(q, t)),[50,51] and transverse current ($C_T(q, t)$).[48,49] The slowly decaying modes considered in different theories include the density, the time derivative of the density, and the longitudinal and transverse currents.

MC has been applied successfully to the study of supercooled liquids and glasses, as well as dense gases and high temperature liquids.[12] However, applications of MC to liquids near their melting point are still limited. MC formalisms were modified subsequently to include the short-time behavior of liquids.[29,32,52] This behavior is governed mainly by binary collisions, although it can also include couplings with fast-decaying modes.

1. Single-particle dynamics

Pioneering work by Levesque and Verlet on dense Lennard-Jones (LJ) fluids with classical MD simulations[53] concluded that the memory function of the VACF, K(t), is described well by the expression

$$K(t) = A \cdot \exp\left(-at^2\right) + Bt^4 \cdot \exp(-bt), \tag{16}$$

where the left and right terms represent the decaying at short and long times, respectively.

Later work by Sjögren, Sjölander, and Wahnström,[29,32,52] based on kinetic and MC theories, generalized Eq. (16) into a binary collision term and an MC term. The coupling term was modified to consider coupling with different density and current modes, while the binary term maintained the expression of a Gaussian function recovering the full value and decay at the time origin of K(t). This decomposition by Sjögren, Sjölander, and Wahnström stimulated applications of MC to liquids such as other LJ fluids, alkalis, *l*-Pb, *l*-Sn, and *l*-Ge.[29,31,52,54–63] However, although the formulation worked successfully for LJ fluids and alkalis, it generally failed for non-simple fluids such as *l*-Pb, *l*-Sn, and *l*-Ge. A different approach to obtain the decay modes of Z(t) was developed by Gaskell and Miller,[64,65] who considered a "velocity field" of the system and analyzed how it was influenced by both $C_L(q, t)$ and $C_T(q, t)$ using MC concepts. Gaskell and Miller's process led to an integral formula for Z(t),

$$Z_{GM}(t) = \frac{1}{24\pi^3} \int f(q) F_s(q, t) \left[C_L(q, t) + 2C_T(q, t)\right], \tag{17}$$

where f(q) is the FT of a normalized function describing the localization of a typical particle, usually taken as the Wigner-Seitz sphere, and $F_s(q, t)$ is the self-intermediate scattering function. The expression for f(q) is

$$f(q) = \left(\frac{3}{\rho}\right) \frac{j_1(aq)}{aq}, \tag{18}$$

where $(4/3)\pi a^3 = 1/\rho$ and $j_1(x)$ is the first-order spherical Bessel function. $F_s(q, t)$ probes single-particle dynamics over different length scales,

$$F_s(q, t) = \frac{1}{N} \left\langle \sum_{j=1}^{N} e^{-i\vec{q}\,\vec{R}_j(t+t_0)} e^{i\vec{q}\,\vec{R}_j(t_0)} \right\rangle. \tag{19}$$

We therefore have applied Gaskell and Miller's formulation to evaluate the decay modes in Z(t). We evaluated the correlations in Eq. (19) for sets of 1000 time steps, taking origins every five time steps.

2. Collective dynamics

The only application of the MC formalism to collective dynamics is based on the Sjögren-Sjölander formalism, where the memory functions of the collective correlation functions are decomposed into slow and fast terms.[29–31] For the longitudinal (transverse) collective dynamics, the decomposition occurs at the level of the second- (first-) order memory function of F(q, t) ($C_T(q, t)$), namely, N(q, t) ($M_T(q, t)$). The final expressions for each term are

$$N(q, t) = N^f(q, t) + N^{MC}(q, t), \tag{20}$$

$$M_T(q, t) = M_T^f(q, t) + M_T^{MC}(q, t). \tag{21}$$

As previously mentioned, there is no specific expression for the binary terms. The only condition is that the short-time characteristics of the memory functions (initial value and first three derivatives) are accounted for. The expression commonly used is a Gaussian ansatz,

$$N^f(q, t) = N(q, 0) \exp\left[-\frac{\left|\ddot{N}(q, 0)\right| t^2}{2N(q, 0)}\right], \tag{22}$$

where $\ddot{N}$ is the second time derivative of N. An equivalent expression is used for $M_T^f(q, t)$.

The expressions for the MC terms are[2,24,30]

$$N^{MC}(q, t) = \frac{\rho k_B T}{8\pi^2 m} \frac{1}{q} \int_0^\infty dk \int_{|q-k|}^{|q+k|} dp \cdot \alpha(q, k, p) \cdot F_n(k, t) F_n(p, t) \left[1 - \frac{F_0(k, t) F_0(p, t)}{F_s(k, t) F_s(p, t)}\right], \tag{23}$$

$$M_T^{MC}(q, t) = \frac{\rho k_B T}{16\pi^2 m} \frac{1}{q} \int_0^\infty dk \int_{|q-k|}^{q+k} dp \cdot \gamma(q, k, p) \cdot F_n(k, t) F_n(p, t) \left[1 - \frac{F_0(k, t) F_0(p, t)}{F_s(k, t) F_s(p, t)}\right], \tag{24}$$

where m is the atomic mass and α and γ are the weight functions,

$$\alpha(q, k, p) = k \cdot p \cdot S(k) S(p) \cdot \left[\frac{q^2 + p^2 - k^2}{2q} \left(\frac{S(k) - 1}{S(k)}\right) + \frac{q^2 + k^2 - p^2}{2q} \left(\frac{S(p) - 1}{S(p)}\right)\right]^2, \tag{25}$$

$$\gamma(q, k, p) = -\frac{k \cdot p \cdot [S(k) - S(p)]^2}{S(p) S(q)} \cdot \frac{(q - k - p)(q - k + p)(q + k - p)(q + k + p)}{4q^2}. \tag{26}$$

Here, k, q, and p denote the wave vectors; S(k) is the static structure factor; and F_n and F_0 are the normalized intermediate scattering function and the binary part of the self-intermediate scattering function, respectively. F_0 is approximated by the free-particle expression

$$F_0(q,t) \equiv \exp\left(-\frac{1}{2m\beta}q^2t^2\right). \quad (27)$$

More details on the formalism can be found in Refs. 2 and 24. Note that the short time behavior of the MC integrals starts as t^4 and consequently the initial value and curvature of the memory functions are determined by the binary terms. These values then are chosen so as to fulfill the exact sum rules up to the sixth moment in the case of F(q, t) and to the fourth moment in $C_T(q,t)$. The next level of sum rules is not imposed, although the results below show that they are satisfied to overall good accuracy.

III. RESULTS AND DISCUSSION

Several properties of *l*-Sn at eight different temperatures were evaluated to test the accuracy of the resulting BLPS, modified with the FM method along with the SM KEDF and the LDA XC functional. At each temperature, we compared the predicted static structure factor S(q), diffusion coefficient, adiabatic sound velocity, and shear viscosity to available experimental and other computational data in Sec. S2 of the supplementary material. Based on this comparison, the overall agreement is reasonable for all of the properties mentioned.

In Subsection III A, we present the collective dynamics of *l*-Sn at 573 K obtained from the OFDFT simulations. In Subsection III B, we apply the MC theory expressions introduced in Sec. II. These results from MC theory then are compared to the OFDFT-MD predictions.

A. Collective dynamics from OFDFT-MD

As mentioned in the Introduction of this paper, Hosokawa *et al.*[18] observed a second mode in the longitudinal dynamics of *l*-Sn in the IXS experiments. Figure 1 displays the comparison of the scattered intensity obtained from OFDFT-MD [Eq. (6)] at 573 K, with the IXS data gathered from Hosokawa *et al.* OFDFT-MD successfully reproduces the collective-dynamics behavior of *l*-Sn when compared to the most recent IXS data.[18] OFDFT-MD correctly recovers the frequencies of the side peaks at both the lowest wave vector [Fig. 1(a)] and highest wave vector [Fig. 1(b)] studied in these IXS experiments. The discrepancy in the region around $\omega = 0$ should not be ascribed directly to a poor representation by OFDFT-MD, because it is a region where the experiment is more sensitive to impurities in the sample. These satisfactory results for $I(q,\omega)$, along with those presented in Sec. S2 of the supplementary material, indicate that OFDFT along with the FM-modified BLPS represent correctly the dynamical behavior of *l*-Sn.

The longitudinal and transverse current correlation functions, $C_L(q,\omega)$ and $C_T(q,\omega)$, respectively, are displayed in Fig. 2. Note that all $C_L(q,\omega)$ displayed in Fig. 2 are calculated as the numerical Fourier transform of Eq. (11), not by using the relationship in Eq. (13). Both $C_L(q,\omega)$ and $C_T(q,\omega)$ at large wave vectors exhibit two modes [Figs. 2(b) and 2(d)]. For $C_L(q,\omega)$, the second mode always appears as a shoulder [Figs. 2(a) and 2(b)], whereas for $C_T(q,\omega)$, there is a wave-vector region where a two-peak shape exists [Figs. 2(c) and 2(d)]. This wave-vector region, where $C_T(q,\omega)$ contains two peaks, is located around the position of the main peak in S(q), $q_p = 2.38$ Å^{-1} (Fig. S2 in the supplementary material). As in previous studies,[20,24] the high frequency mode in $C_T(q,\omega)$ is considered as the second mode due to its abnormal behavior, different from the main transverse mode in one-component liquid metals.

The shape of $S(q,\omega)$ also suggests the existence of a second mode, which is difficult to discern in Fig. 1 due to the convolution with the experimental resolution function. Previous studies comparing the different collective dynamics functions in *l*-Ga[17] and *l*-Sn[18] concluded that the second mode present in $S(q,\omega)$ was caused by a coupling between $S(q,\omega)$ and $C_T(q,\omega)$. This assumption emerged from comparing the location of the second mode in $S(q,\omega)$ to the position of the main peak in $C_T(q,\omega)$; both were located at very similar frequencies for the same wave vectors. However, this assumption violates the condition of orthogonality between the longitudinal and transverse dynamics by assuming a direct coupling between them. A comparison between $S(q,\omega)$ and $C_T(q,\omega)$ at two different wave vectors is displayed in Fig. 3. The main peak of $C_T(q,\omega)$ clearly does not coincide with the second mode in $S(q,\omega)$. Therefore, our results do

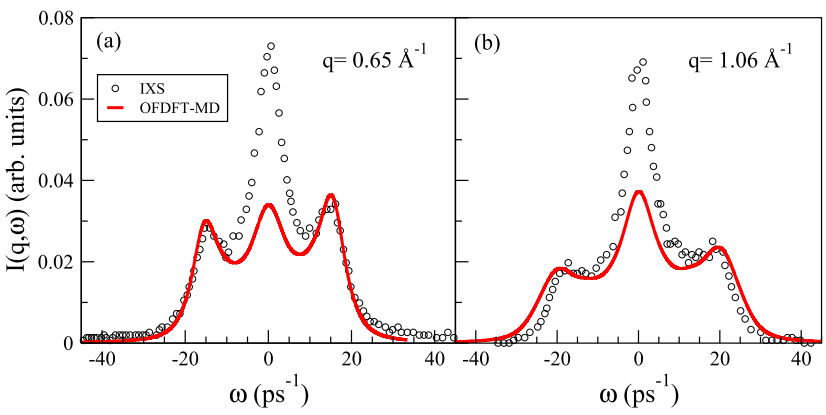

FIG. 1. Scattered intensity I(q,ω) at wave vectors 0.65 Å^{-1} and 1.06 Å^{-1} for *l*-Sn at T = 573 K. Full line: OFDFT-MD results after convolution with the experimental resolution function [Eq. (6)]. Open circles: IXS measurements of Hosokawa *et al.*[18] for wave vectors 0.66 Å^{-1} and 1.06 Å^{-1}.

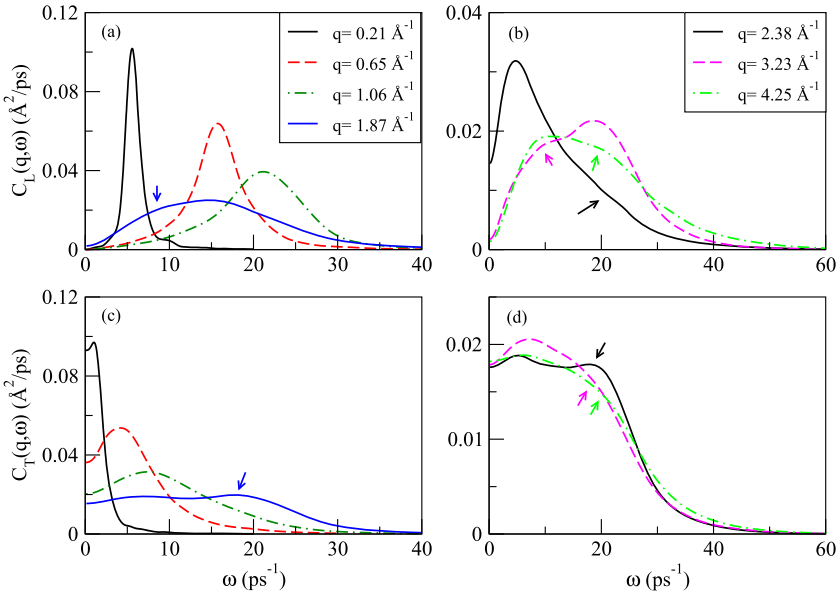

FIG. 2. $C_L(q, \omega)$ and $C_T(q, \omega)$ for several wave vectors. [(a) and (c)] Below $q_p = 2.38$ Å^{-1}. [(b) and (d)] Above q_p. Arrows qualitatively indicate the location of the second mode in each case, either as a shoulder or as a peak.

not support the idea of direct coupling between $S(q, \omega)$ and $C_T(q, \omega)$ as the origin of the second mode in the longitudinal dynamics.

For different wave-vector regions, $S(q, \omega)$, $C_L(q, \omega)$, and $C_T(q, \omega)$ each exhibit a peak at a characteristic frequency, denoted as ω_m, ω_L, and ω_T, respectively. For example, in Fig. 1, ω_m appears at a frequency of 15.1 ps^{-1} at q = 0.65 Å^{-1} and increases with the wave vector to 19.56 ps^{-1} at q = 1.06 Å^{-1}. The dispersion relation of ω_m with q is displayed in Fig. 4, along with the dispersion relations of ω_L and ω_T. The dispersion relation of $S(q, \omega)$ follows a very similar shape as that of $C_L(q, \omega)$ at small wave vectors (q < 0.8 Å^{-1}). However, as the wave vectors increase, so does the difference between both sets of dispersion relations. This difference between the dispersion relations of $S(q, \omega)$ and $C_L(q, \omega)$ is due to their relationship as implied by Eq. (13). This relationship in reciprocal space translates into $C_L(q, \omega) = (\omega/q)^2 S(q, \omega)$. As the wave vector increases, the peak frequency in $S(q, \omega)$ increases in a way that (ω/q) always increases, causing a shift to higher frequencies for the maxima of $C_L(q, \omega)$ with respect to those of $S(q, \omega)$. The most important result displayed in Fig. 4 is the existence of two branches in the dispersion relation of $C_T(q, \omega)$ for wave vectors around q_p (= 2.38 Å^{-1}). These two frequency branches, due to the existence of two peaks in $C_T(q, \omega)$, represent the two modes present in transverse dynamics. The lower frequency branch represents the main propagating mode in $C_T(q, \omega)$ due to shear wave propagation, while the high-frequency mode still has an unknown origin. In addition, as in previous studies of this second mode in different systems,[20,23,24] the frequency value where the second mode of $C_T(q, \omega)$ appears is close to the highest frequency value of $C_L(q, \omega)$'s main mode.

As noted in Sec. II C, the propagating modes in $S(q, \omega)$, $C_L(q, \omega)$, and $C_T(q, \omega)$ do not always appear as maxima; for most wave vectors, their appearance takes the form of a shoulder. We therefore use the fitting model composed of Eqs. (14) and (15) in order to study the dispersion relation of each propagating mode in each direction. The resulting dispersion relations (*vide infra*) show that while the main mode in $C_T(q, \omega)$ always corresponds to the low-frequency branch, in $C_L(q, \omega)$ the main mode oscillates between the high-frequency branch (specifically for $q < 2.0$ Å^{-1} and $q > 3.0$ Å^{-1}) and low-frequency branch (for 2.0 Å^{-1} < q < 3.0 Å^{-1}).

B. MC theory

1. Single-particle dynamics

We use the MC approximation of Gaskell and Miller[64,65] to study the VACF and its decomposition into the longitudinal

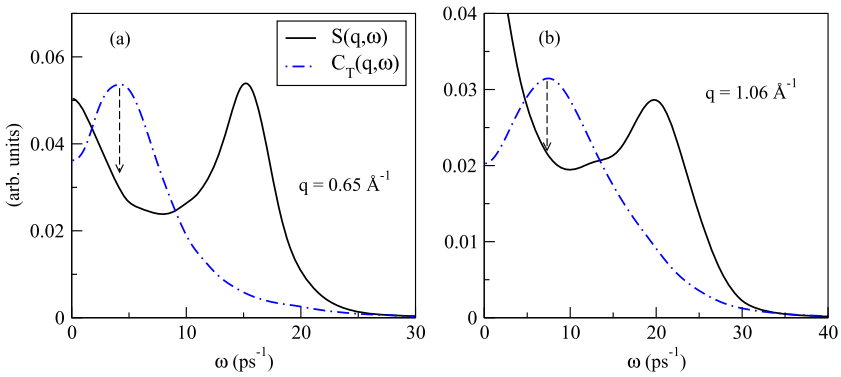

FIG. 3. $S(q, \omega)$ (full line) and $C_T(q, \omega)$ (dash-dotted line) for two wave vectors. $S(q, \omega)$ is scaled so as to fit in the same graph. The vertical lines with arrows denote the position of the maximum of $C_T(q, \omega)$ and where its effect on the shape of $S(q, \omega)$ should be located in the case of direct coupling.

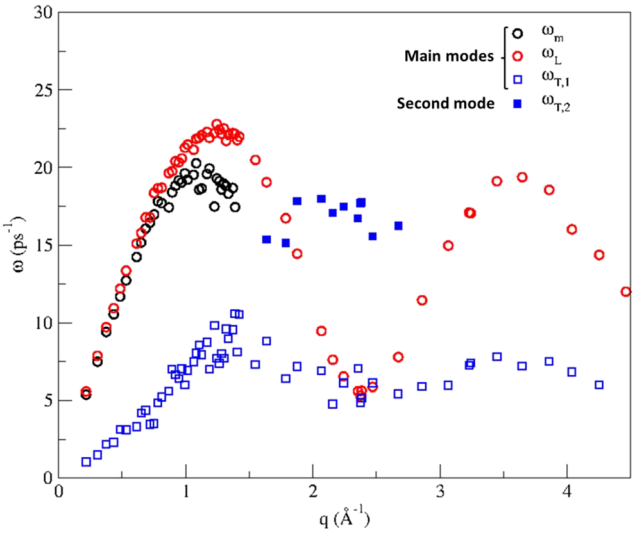

FIG. 4. Dispersion relations for *l*-Sn at T = 573 K obtained directly from OFDFT-MD simulations. S(q, ω) (black circles) displays the same initial dispersion relation as $C_L(q, \omega)$ (red circles). S(q, ω) displays side peaks (ω_m) up to wave vectors ~1.4 Å^{-1}. Above that limit, the diffusive component completely covers the dispersive component. $C_T(q, \omega)$ (blue squares) exhibits two dispersion branches. The second mode in $C_T(q, \omega)$ ($\omega_{T,2}$), only visible in a small wave-vector range, is displayed as filled squares.

and transverse components, as described by Eq. (17). The resulting VACFs from OFDFT-MD data and the MC expressions are plotted in Fig. 5. The shape of the VACF ($Z_{OFDFT-MD}$) from OFDFT-MD exhibits the typical behavior for liquid metals. For long times compared to the microscopic relaxation times, the initial and final velocities are completely uncorrelated, with $Z(t \to \infty) = 0$. For short times, the decaying of Z(t) depends on the density and temperature. In a high-density liquid such as *l*-Sn, Z(t) exhibits a very fast decay with damped oscillations. This phenomenon, called the "cage effect," occurs because each Sn atom is surrounded by neighbors, and its movement consists of collisions with them inside

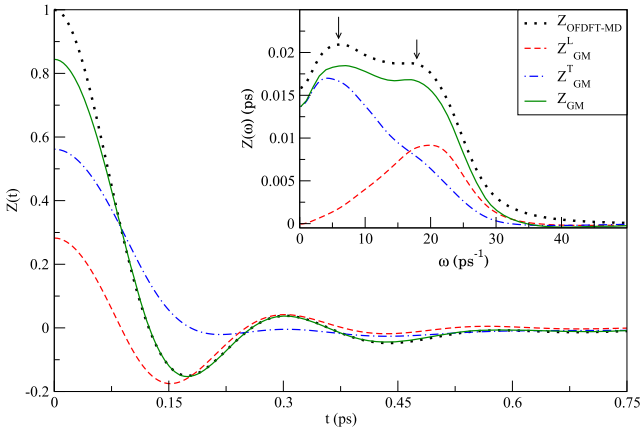

FIG. 5. Normalized VACF, Z(t), obtained from OFDFT-MD of *l*-Sn at T = 573 K (circles). The inset shows the power spectrum Z(ω). Dashed and dash-dotted curves represent the longitudinal Z^L_{GM} and transverse Z^T_{GM} components, respectively, of the total $Z_{GM}(t)$ and $Z_{GM}(\omega)$ (continuous line). Arrows indicate the two peaks in the power spectrum, each attributable to a different type of the collective dynamics via Gaskell and Miller's MC formulation [Eq. (17)].

this cage.[1,2] $Z_{OFDFT-MD}$ and the MC-calculated VACF (Z_{GM}) agree very well overall. Very short-time values differ somewhat due to the limited integration range available from the OFDFT-MD simulations, but the recovery of the negative minimum and subsequent damped oscillations is excellent. The inset of Fig. 5 depicts the power spectrum obtained from the OFDFT-MD data and from Gaskell and Miller's MC formalism. Both power spectra have two peaks, although Gaskell and Miller's is shifted slightly downwards. Decomposition of the power spectrum via Eq. (17) allows us to interpret each of the two peaks as originating from longitudinal (Z^L_{GM}) and transverse (Z^T_{GM}) contributions.

The shape of the power spectrum is closely related to the extent to which a second mode is observed in a system's collective dynamics. The power spectrum decomposition using Gaskell and Miller's approach was also utilized by Marqués *et al.*[22] They performed OFDFT-MD simulations of *l*-Na in a similar way, although in their case they considered pressures ranging from 0 to 100 GPa. They found no evidence of a second mode at zero pressure. However, when the pressure was increased to 45 GPa, a second mode emerged in both $C_L(q, \omega)$ and $C_T(q, \omega)$ around wave vectors close to q_p. The wave-vector region where this second mode became visible increased with pressure. Marqués *et al.* predicted the power spectrum to have just one peak at zero pressure, with the longitudinal component of Z(ω) completely covered by the transverse component. Both components started to separate as the pressure increased to 45 GPa and two distinguishable peaks appeared. Therefore, the VACF and power spectrum of *l*-Sn at zero pressure paint a similar picture to that of *l*-Na at high pressures; this is in accordance with *l*-Sn presenting a second mode at zero pressure, whereas *l*-Na only exhibits the second mode at high pressures. In our previous work on MC in *l*-Zn,[24] the power spectrum was also evaluated directly from the simulation data using Gaskell and Miller's MC theory. The results obtained for *l*-Zn closely resemble *l*-Sn's; the two separated peaks in the power spectrum, the higher-frequency peak attributed to longitudinal dynamics, and the lower-frequency peak ascribed to transverse dynamics (Fig. 5). This observed trend in the power spectrum of *l*-Sn and *l*-Zn, together with that of *l*-Na at high pressures, strongly suggests that the appearance of a second mode in the collective dynamics is connected to the separation of both longitudinal and transverse components of the power spectrum.

An equivalent relationship can be extracted from the shape of the power spectrum of *l*-Sn and the dispersion relations of $C_L(q, \omega)$ and $C_T(q, \omega)$ (Fig. 4). The decomposition of the power spectrum of *l*-Sn illustrates the main frequencies at which Sn atoms oscillate in the liquid and separates them into a longitudinal main mode around a frequency of 20 ps^{-1} and a transverse main mode around a frequency of 5 ps^{-1}. While the frequency range for longitudinal and transverse dispersion relations spans a wide region, the maxima at each wave vector tend to concentrate in certain frequency ranges. Consequently, these frequency ranges appear as wide peaks in the power spectrum. Figure 6 provides a comparison between the range of frequencies of the wide peaks in the power spectrum's decomposition and the frequencies in the dispersion relations of both modes in $C_L(q, \omega)$ and $C_T(q, \omega)$, obtained

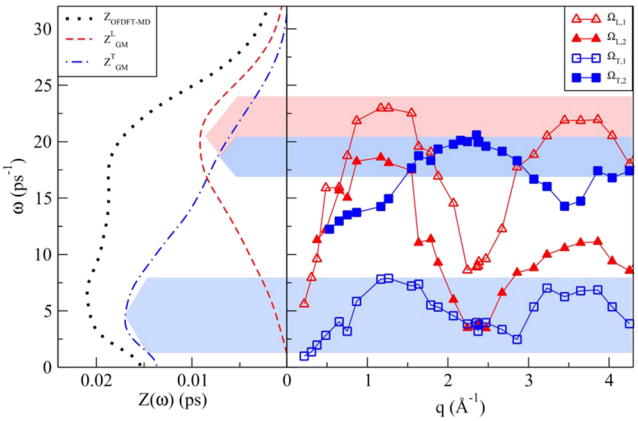

FIG. 6. Relationship between the maxima and shoulders of the longitudinal and transverse components of the power spectrum as computed by MC theory, Z^{L}_{GM} and Z^{T}_{GM}, respectively (left panel), and the frequencies of the dispersion curves of each mode in the longitudinal ($\Omega_{L,1}$ and $\Omega_{L,2}$ as triangles) and transverse ($\Omega_{T,1}$ and $\Omega_{T,2}$ as squares) directions, obtained using the fitting model described in Eqs. (14) and (15). We distinguish here between the frequencies of the maxima from the MDHO, Ω_L and Ω_T, and the frequencies of the maxima of the collective dynamics obtained directly from the MD results, ω_L and ω_T. The horizontal red shaded arrow encompasses the side peaks in $C_L(q,\omega)$ that contribute to the main peak in Z^{L}_{GM}. Likewise, the two horizontal blue shaded arrows encompass the side peaks in $C_T(q,\omega)$ [Figs. 2(c) and 2(d)], each related to a different mode. The low-frequency arrow indicates the contributions of the main transverse mode to the peak in Z^{T}_{GM}. The high-frequency arrow indicates the contributions of the second transverse mode to the shoulder at high frequencies in Z^{T}_{GM}.

with the fitting model of Sec. II C. The shaded arrows in Fig. 6 illustrate how the concentration of the main modes in each frequency range account for both peaks in the power spectrum of *l*-Sn. Moreover, the shoulder present in Z^{T}_{GM} at frequencies around 18.5 ps^{-1}, close to the peak of Z^{L}_{GM}, may stem from the second mode in $C_T(q,\omega)$ (high-frequency blue arrow). The second mode in $C_L(q,\omega)$ does not have such a clear impact on the longitudinal component of the power spectrum of *l*-Sn; the longitudinal component does not exhibit any visible shoulder. The reason for this lack of visible influence is probably due to the proximity of the frequency of the second mode to the main mode in longitudinal dynamics. This proximity between modes results in the second mode always appearing as a shoulder in $C_L(q,\omega)$. Overall, the information extracted from Gaskell and Miller's decomposition of the power spectrum can help to determine whether to expect second peaks and their frequency ranges.

2. Collective dynamics

We apply the Sjögren-Sjölander MC scheme [Eqs. (20)–(27)] to verify whether MC theory is able to predict the second mode obtained in the collective dynamics of *l*-Sn. Figure 7 shows $S(q,\omega)$ and $C_L(q,\omega)$ at different wave vectors, obtained from OFDFT-MD and from Sjögren and Sjölander's MC formulation. $S(q,\omega)$ is displayed at wave vectors smaller than $q_p/2$, where the second mode is observed clearly and not covered by the diffusive component. Likewise, $C_L(q,\omega)$ is displayed for wave vectors higher than $q_p/2$, where the second mode starts to be visible. Figure 8 displays analogous data for the transverse component, $C_T(q,\omega)$. Figures 7 and 8 illustrate that the MC theory does a fair job of reproducing the two modes and their positions in both $C_L(q,\omega)$ and $C_T(q,\omega)$, as obtained from OFDFT-MD.

MC theory also provides an explanation for the frequencies of both modes of $C_T(q,\omega)$ and its limited dispersion. In Eq. (24), the weight of the coupling at each wave vector is determined by the function $\gamma(q,k,p)$, detailed in Eq. (26). Because of the structural term $[S(k) - S(p)]^2/[S(k)S(p)]$ in Eq. (26), maxima will appear for those pairs of wave vectors related to a small value of the structure factor and large differences between S(k) and S(p). These pairs of wave vectors correspond to cases where $k \to 0$ and p is close to q_p and *vice versa*, with $p \to 0$ and k close to q_p, due to the symmetry of the function. Figure 9 displays the dependence of $\gamma(q,k,p)$ on the wave vectors k and p for four wave vectors: the smallest attainable wave vector determined by the simulation box size, around $q_p/2$, around q_p, and beyond q_p. Recall

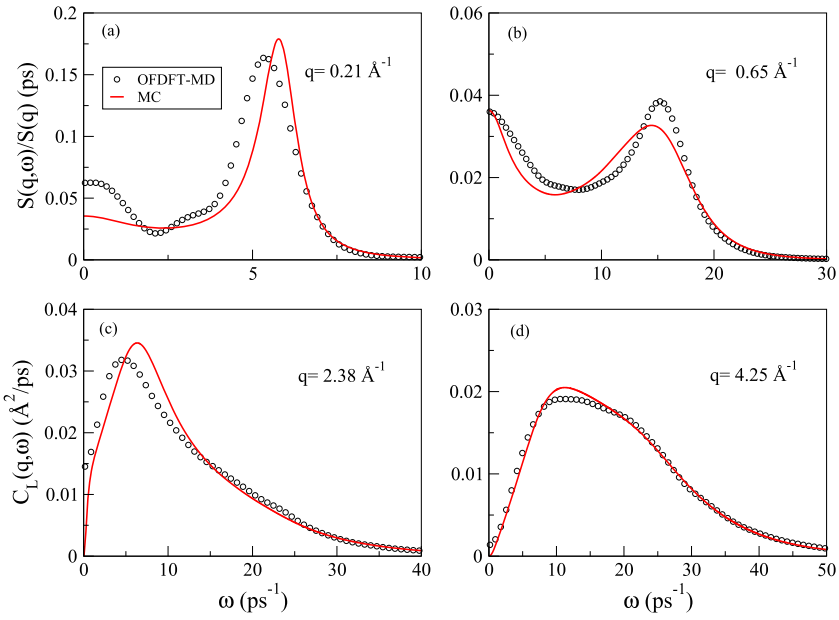

FIG. 7. [(a) and (b)] Dynamic structure factors at wave vectors below $q_p/2$. [(c) and (d)] Longitudinal current correlation spectra at wave vectors above $q_p/2$. Circles: OFDFT-MD simulations. Solid Curves: Sjögren and Sjölander's MC theory.

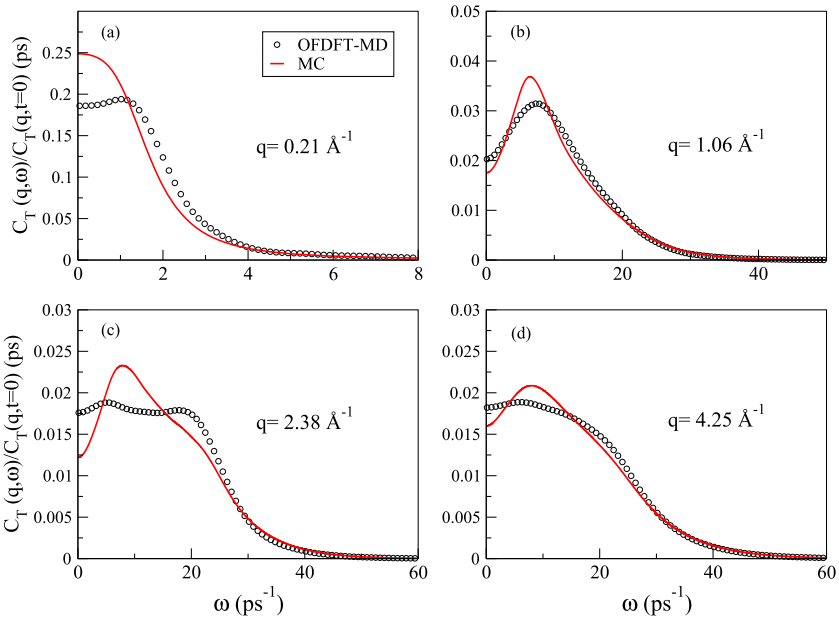

FIG. 8. Predicted transverse current correlation spectra at different wave vectors. Circles: OFDFT-MD simulations. Solid curves: Sjögren and Sjölander's MC theory.

that the second mode of $C_T(q, \omega)$ was most visible in the intermediate region between $q_p/2$ and around q_p. In this region, $\gamma(q, k, p)$ always exhibits maxima for approximately the same wave vector, $k = q_p$ and $p = q_p/2$ [Figs. 9(b) and 9(c)]. This fixed position of the maxima explains the small dispersion in both modes of $C_T(q, \omega)$ in the region between $q_p/2$ and around q_p (Figs. 4 and 6). Moreover, the frequencies of both modes of $C_T(q, \omega)$ in this intermediate region correspond to the frequencies of the longitudinal modes in q_p and $q_p/2$, which are the wave vectors for the maxima of $\gamma(q,k,p)$. Hence, we not only explain through MC the appearance of the second mode in $C_T(q, \omega)$, but also its small dispersion and magnitude of its frequencies.

Next, we perform a test to assess if the existence of the second mode is entirely due to MC. It can be argued that MC reproduces the two-mode shape because both modes already exist in the input functions used in the MC expressions. However, if a two-mode shape is obtained with MC, using as input

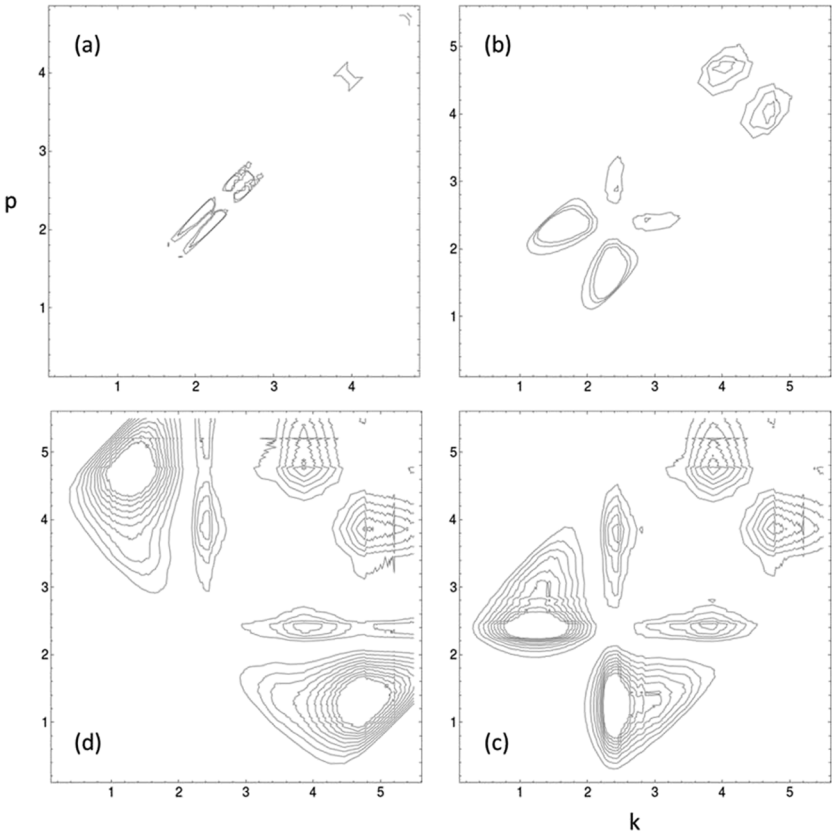

FIG. 9. Isolines for the weight function $\gamma(q, k, p)$ at $q = 0.21$ (a), 1.06 (b), 2.38 (c), and 4.25 (d) Å^{-1}. The contours are plotted every 1.5 units for (a) and every 25 units for (b)–(d). The clockwise ordering of the panels is deliberate, to make it easier to see that the main contribution at $k \sim 2.3$ does not change from panels (b) to (c), which explains why the second mode is not dispersive.

one-mode functions, then one could conclude unequivocally that the origin of the two-mode shape is MC. In both MC expressions [Eqs. (23) and (24)], the input functions that effectively introduce the two-mode shape are mainly the $F_n(q,t)$ s. The $F_s(q,t)$ s all have diffusive character, and the $F_0(q,t)$ s are all modelled with a Gaussian function [Eq. (27)]; neither main nor secondary modes are present in any of the $F_s(q,t)$ s or $F_0(q,t)$ s, or, if they are present, their amplitude is very small compared to the diffusive mode and therefore they have no meaningful contribution. To eliminate the second mode in the $F_n(q,t)$ s, we used the already fitted expressions of both $F(q,t)$ and $C_L(q,t)$ to Eqs. (14) and (15), but without considering the term corresponding to the second mode. Afterwards, the new $F(q,t)$ s obtained are normalized and used in the calculation of the MC terms. Figure 10 shows the resulting spectra for both the longitudinal and transverse directions at two wave vectors where the two-mode shape was identified clearly.

As can be observed in Fig. 10, MC still reproduces the two-mode shape even when the functions used as input have only one mode. We previously explained the existence of two transverse modes and their frequencies by only appealing to the frequency of the main modes in the input functions as suggested by Fig. 9. However, this last test definitely proves that the origin of the second mode in both the longitudinal and transverse directions is due to an indirect coupling between the main modes.

Nevertheless, limitations to MC theory still persist. Specifically, when MC is applied to the longitudinal direction, the results from the theory do not exhibit the characteristic second mode as seen in the OFDFT-MD results for $S(q,\omega)$ at small wave vectors, as shown in Fig. 7(a). In the transverse direction, the results obtained from MC theory do not reproduce the amplitude of either mode from OFDFT-MD in the wave-vector region close to $q_p = 2.38$ Å^{-1} [Fig. 8(c)]. Moreover, there is a general overestimation of the main mode in the transverse dynamics [Fig. 8]. An improvement in the applicability of MC comes from a detailed study of the expressions used by Sjögren and Sjölander in their formulation to represent the memory functions, $N(q,t)$ and $M_T(q,t)$. Figures 11 and 12 illustrate $N(q,t)$ and $M_T(q,t)$, respectively. Each memory function is depicted for two different wave vectors (below and around q_p), obtained directly from the simulation data (OFDFT-MD) and from MC theory (N_{orig} and $M_{T,orig}$). Two defects common to both $M_T(q,t)$ and $N(q,t)$ are evident: (1) failure of the MC theory to recover the negative minima present at wave vectors close to q_p and (2) overestimation of the tail at long times [Figs. 11(d) and 12(d)]. Previous attempts to apply the Sjögren-Sjölander MC theory to different liquid metals encountered similar shortcomings. Gudowski *et al.*[55] applied MC theory to analyze a classical MD-derived VACF of *l*-Pb, using the Sjögren-Sjölander formulation based on the Levesque-Verlet empirical form[53] valid for a LJ system. Gudowski *et al.* demonstrated the failure of MC to recover the characteristic negative minimum of the VACF. They provided some explanations for this limitation, the most plausible being an incorrect representation of the binary part. Gudowski *et al.* proposed a modification to the theoretical expression,[55] namely, adding a negative term with coefficients fitted to correctly recover such negative minima. In our study of *l*-Sn, the negative minimum in the VACF is perfectly recovered by using Gaskell and Miller's MC formulation, as shown in Fig. 5. However, Gaskell and Miller's MC approach has only been developed thus far for single-particle dynamics, not collective dynamics. We therefore propose, as an improvement to Sjögren-Sjölander's MC theory, a new expression for the binary term based on the VACF. Improvements in the long-time tail may come by coupling with further modes such as energy density, e.g., in Bryk *et al.*'s work on *l*-Li.[20] However, such a study is beyond the scope of this work, so here we can only consider improvements to the representation of the (short-time) binary term.

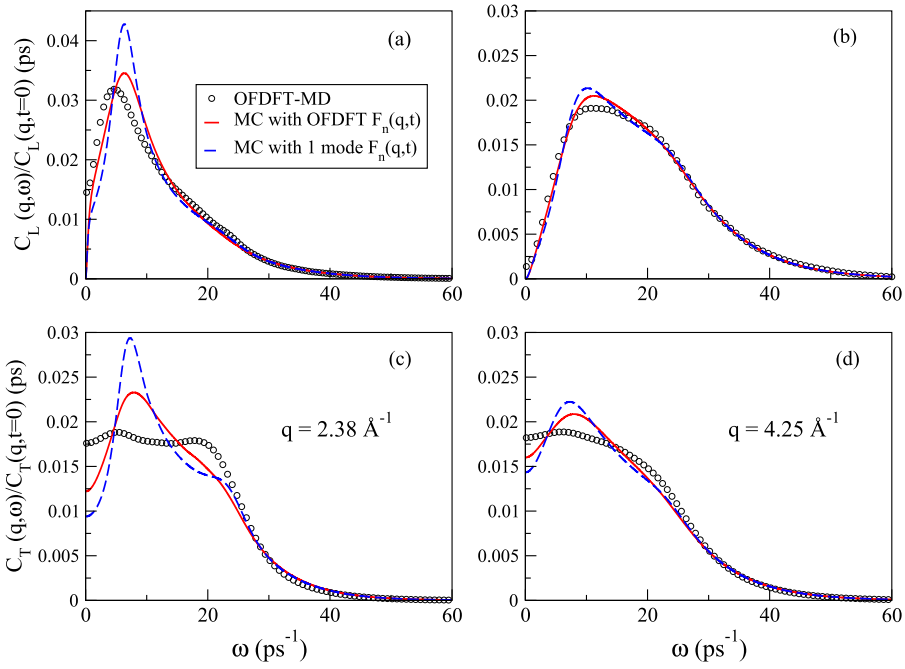

FIG. 10. OFDFT-MD-calculated $C_L(q,\omega)$ [(a) and (b)] and $C_T(q,\omega)$ [(c) and (d)] (circles), along with MC theory results using the OFDFT-MD $F_n(q,t)$ (continuous line) and the one-mode $F_n(q,t)$ (dashed line) for wave vectors 2.38 Å^{-1} [(a) and (c)] and 4.25 Å^{-1} [(b) and (d)].

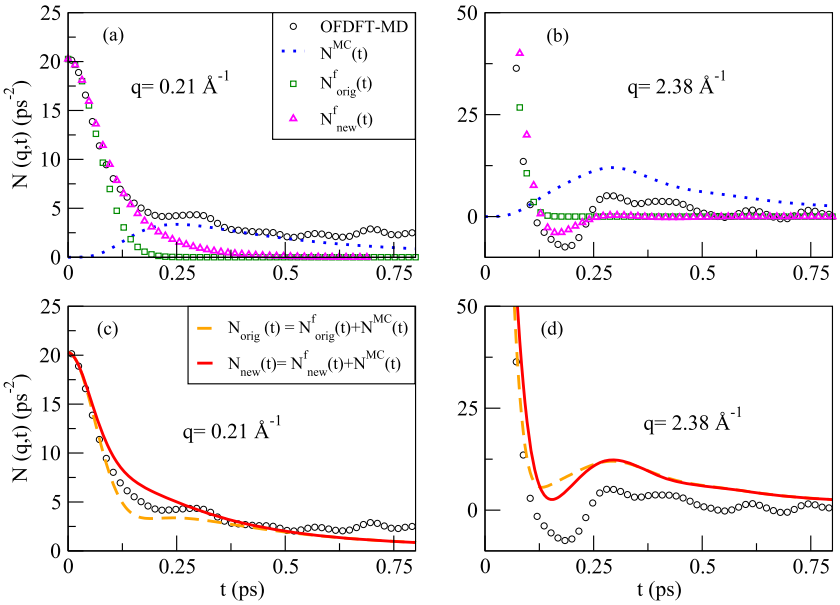

FIG. 11. N(q, t) for two wave vectors: below q_p (0.21 Å^{-1}) and around q_p (2.38 Å^{-1}). Circles: OFDFT-MD. Dotted curves: MC component [Eq. (23)]. Squares: Original binary term [Eq. (22)]. Triangles: New binary term [Eq. (29)]. Dashed curves: Total N(q, t) with the original expressions. Continuous curves: Total N(q, t) with the new binary term.

An analysis of the OFDFT-MD-derived memory functions reveals that for all wave vectors where the minimum exists, it is located around the same value of t as the backscattering minimum of Z(t). Moreover, this minimum becomes shallower as the wave vector is decreased, eventually disappearing. As mentioned earlier, there is no specific reason for the choice of the binary term expression, and the only requirements consist of recovering correctly the t = 0 values of both the N(q, t) and M_T(q, t) functions and its second time-derivatives.[31] Because of the apparent relation between the power spectrum and the current dispersion relations discussed earlier, we modified the theoretical ansatz used for the fast part of the memory functions so as to include the VACF. However, the VACF first had to be modified to correctly represent the amplitude of the negative minima found in the simulations. We constructed a "modified" VACF by smearing Z(t) via a convolution with a q-dependent function whose width increases for smaller wave vectors, leading to shallower (and wider) minima as the wave vector decreases without changing its position. The expression we have chosen is (in the frequency domain)

$$Z^*(q,\omega) = Z(\omega)\cdot\exp\left(-\frac{\omega^2}{c_s^2 q^2}\right), \tag{28}$$

where c_s is the velocity of sound in the system. This modification does not imply any fitting of any kind and can, in principle, be applied to any system. The corresponding $Z^*(q, t)$ then is inserted into the ansatz, taking care to recover the initial values and decay rates of the total memory function as required by the MC theory, namely,

$$N^f(q,t) = \frac{N_0}{1+\frac{1}{2}\left(\frac{|\ddot{N}_0|}{N_0}-\omega_E^{*2}(q)\right)t^2}\cdot Z^*(q,t), \tag{29}$$

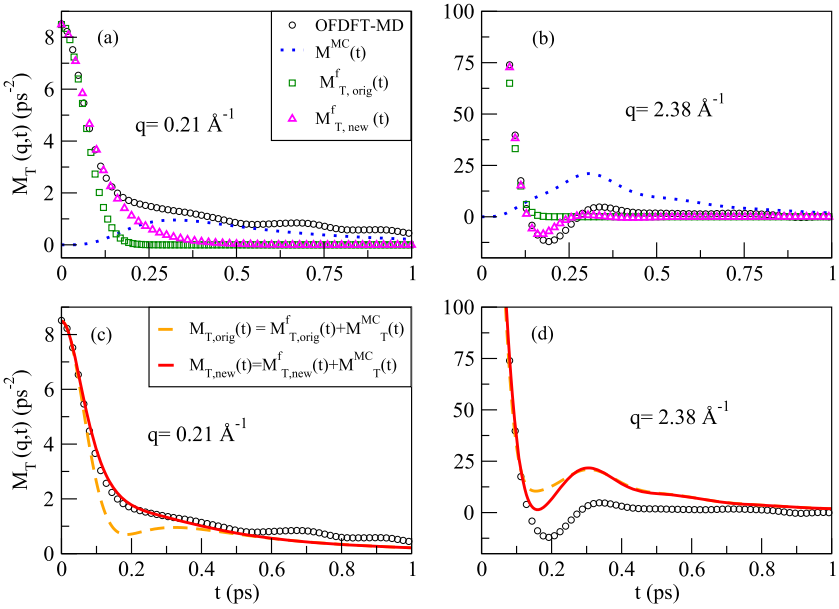

FIG. 12. M_T(q, t) for the same two wave vectors as in Fig. 11. Circles: OFDFT-MD. Dotted curves: MC component [Eq. (24)]. Squares: Original binary term [Eq. (22)]. Triangles: New binary term [Eq. (29)]. Dashed curves: Total M_T(q, t) with the original expressions. Continuous curves: Total M_T(q, t) with the new binary term.

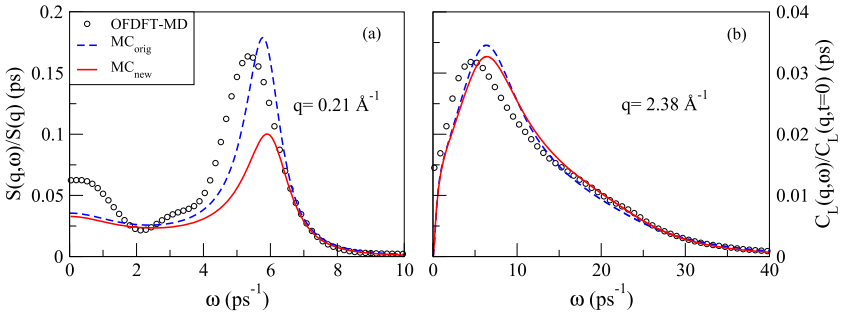

FIG. 13. $S(q,\omega)$ (left panel) and $C_L(q,\omega)$ (right panel) calculated directly from OFDFT-MD (circles) and from MC theory with the original [Eqs. (22) and (23)] and new binary [Eqs. (23) and (29)] terms, shown by dashed and solid curves, respectively, at two different wave vectors. Values on the vertical axes are normalized to the value at the sampling time origin.

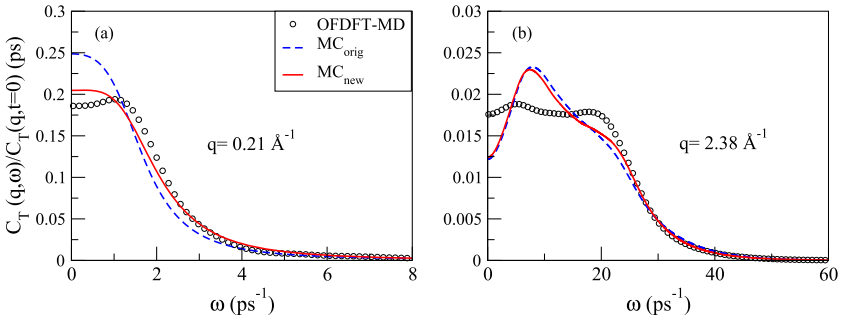

FIG. 14. $C_T(q,\omega)$ calculated directly from OFDFT-MD (circles) and from MC theory with the original [Eqs. (22) and (24)] and new binary [Eqs. (24) and (29)] terms, shown by dashed and solid curves, respectively, at two different wave vectors.

where $\omega_E^*(q)$ is the "Einstein frequency" of $Z^*(q,t)$, obtained from its short-time expansion,

$$Z^*(q,t) = 1 - \omega_E^{*2}(q)t^2/2 + \cdots . \tag{30}$$

Figures 11 and 12 compare the representations of $N(q,t)$ and $M_T(q,t)$, respectively, obtained by applying the Sjögren-Sjölander MC approach with the Gaussian ansatz and our new expression for the binary term [Eq. (29)]. On the whole, the results are improved by using our proposed expression for the binary term. For both $N(q,t)$ and $M_T(q,t)$, at small wave vectors [Figs. 11(a) and 12(a)], the new respective binary expressions (N^f_{new} and $M^f_{T,new}$) have a decay rate more similar to OFDFT-MD than the original Gaussian ansatz (N^f_{orig} and $M^f_{T,orig}$). At large wave vectors [Figs. 11(b) and 12(b)], the new binary expressions correctly introduce the negative minima. However, while the position of the negative minimum is correct with the new binary expression, the amplitude is incorrect. Overall, the amplitudes of the minima obtained with the new binary expression are underestimated, resulting in an even greater underestimation of the minima once the MC term is added. Yet, the sum of the new binary expression with the MC term improves the final representation in most cases. For $N(q,t)$ at a small wave vector [Fig. 11(c)], the final expression overestimates the OFDFT-MD results in the same magnitude as the original expression underestimates them.

We further test the new binary expression by analyzing $C_L(q,\omega)$ and $C_T(q,\omega)$. Figures 13 and 14 display $C_L(q,\omega)$ and $C_T(q,\omega)$, respectively, obtained from OFDFT-MD, along with MC theory using the Gaussian ansatz (MC_{orig}) and our new expression (MC_{new}) for the binary terms. In the longitudinal direction at the small wave vector [Fig. 13(a)], our new binary term offers no improvement in $S(q,\omega)$. At high wave vectors, the improvement in the recovery of the minimum in Fig. 11(d) by using the new binary term translates into a minor improvement of $C_L(q,\omega)$ [Fig. 13(b)]. In the transverse direction, recovery of $C_T(q,\omega)$ for the small wave vector is exceptional [Fig. 14(a)]. However, at the high wave vector [Fig. 14(b)], only a minor enhancement is seen for the amplitude of the second mode located around 20 ps^{-1}. Overall, improvements in $C_L(q,\omega)$ and $C_T(q,\omega)$ using the new binary expression are less significant than expected, which indicates that further modifications to the theory are needed. Nevertheless, the new binary expression does not modify qualitatively the two-mode shape obtained with MC theory; the existence of the second mode thus is due entirely to the MC term.

IV. CONCLUSIONS

OFDFT-MD simulations can offer insight into the complex collective dynamics present in liquid metals. Complicated longitudinal dynamics in *l*-Sn was observed previously by IXS measurements. Here, we predicted that these complex dynamics are present not only in the longitudinal direction but also in the transverse direction at higher wave vectors, in the kinetic regime. These complex transverse collective dynamics arise as a second collective mode in the spectra of the transverse currents, $C_T(q,\omega)$.

Although the existence of the complex collective dynamics had been observed experimentally and computationally in a variety of liquid metals, a theoretical explanation remains unclear. Previously, two of the authors proposed MC as the origin of the complex collective dynamics present in *l*-Zn.[24] Further applications of MC theory to more liquids with the complex collective dynamics were needed to verify this proposal. Here, we showed that MC can indeed help explain the complex collective dynamics of *l*-Sn: the theory predicted that a second mode is present in both the longitudinal and

transverse collective dynamics and indicated that it arises via indirect coupling of the transverse and longitudinal modes. Thus, MC may be the best theoretical framework to explain the complex collective dynamics observed in several liquid metals.

Nevertheless, improvements in MC theory are needed to reproduce simulation data. Similar differences between simulation and MC data arose in the earlier study of *l*-Zn and therefore were probably a general limitation of the theory. As a first modification toward a more general MC approach, we proposed and tested a new expression for the binary term used in the Sjögren-Sjölander MC formulation of the collective dynamics. This new binary term offers some improvement, especially for low wave vectors in the transverse collective dynamics. Further improvements could be made by introducing transverse dynamics into the MC term of N(q, t) and considering couplings with other modes besides density modes, such as energy density.

In closing, we provided a theoretical explanation for the appearance and behavior of a second mode in the collective dynamics of *l*-Sn. Along with the previous study of *l*-Zn, MC theory proves to be a successful theoretical framework to explain this new feature observed in the collective dynamics of various liquid metals.

SUPPLEMENTARY MATERIAL

See supplementary material for details concerning the creation of the Sn LPS (Sec. S1) and the calculation of various thermodynamic, structural, and transport properties of liquid Sn in the range of temperatures from 573 K to 1873 K (Sec. S2). Details on the sets of configurations and time origins used for the evaluation of different collective dynamic functions are provided in Sec. S3.

ACKNOWLEDGMENTS

This work was supported by the Office of Naval Research (Grant No. N00014-15-1-2218) to E.A.C. and by MECD Grant No. FIS2014-59279-P and European regional FEDER funds to L.E.G. B.G.R. gratefully acknowledges financial support from Universidad de Valladolid for a Ph.D. scholarship and an exchange scholarship. The authors thank the Computational Science and Engineering Support (CSES) group at Princeton University for maintaining the Terascale Infrastructure for Groundbreaking Research in Science and Engineering (TIGRESS). The authors also thank Dr. Gilles Tarjus for very useful discussions. The authors are indebted to Ms. Nari Baughman for careful editing and to Dr. Johannes M. Dieterich and William C. Witt for critical reading of this manuscript.

APPENDIX: MEMORY FUNCTIONS

The study of the mechanisms determining the liquid state's collective dynamics requires a formalism that can be applied correctly to any temporal and spatial regions. In the hydrodynamic regime, the liquid state can be pictured as a continuum where density fluctuations displace it away from its equilibrium state. In this regime, the relaxation modes ruling the decay of these density fluctuations can be analyzed by using equations that govern the system at this scale and by obtaining the corresponding correlation functions. However, when times are reduced (or frequencies increased), the hydrodynamic approach starts to fail due to the presence of dissipative terms in the basic hydrodynamic equations, which are not invariant under time reversal. Therefore, instead of discarding the equations directly, it was decided to generalize them while still maintaining the basic ideas. This generalization is based on making the response of the system sensitive to perturbations in the temporal and spatial scales.

One of the most successful formalisms used is that of the projection operators introduced by Zwanzig and Mori.[66–68] It poses an equation of motion for the correlation function,

$$\dot{C}(t) = -\int_0^t K(\tau)\, C(t-\tau)\, d\tau, \tag{A1}$$

where K(t) is the memory function of C(t). The solution of Eq. (A1) in Laplace space is

$$\tilde{C}(z) = \frac{C(0)}{z + \tilde{K}(z)}, \tag{A2}$$

where the tilde denotes the Laplace transform.

The memory function also obeys a Langevin equation with a self-memory function, called $K_1(t)$, in such a way that

$$\dot{K}(t) = -\int_0^t K_1(\tau)\, K(t-\tau)\, d\tau \quad \Rightarrow \quad \tilde{K}(z) = \frac{K(0)}{z + \tilde{K}_1(z)}, \tag{A3}$$

where $K_1(t)$ is the second-order memory function of C(t). The process can be iterated *ad infinitum*, with the correlation function being expressed as a continuous fraction,

$$\tilde{C}(z) = \frac{C(0)}{z + \frac{K(0)}{z + \frac{K_1(0)}{z + \cdots}}}. \tag{A4}$$

We have employed this representation to study the theoretical models used by the MC theory for both the longitudinal and transverse current correlation functions throughout the paper.

[1] J. P. Hansen and I. R. McDonald, *Theory of Simple Liquids* (Academic Press, London, 1986).
[2] U. Balucani and M. Zoppi, *Dynamics of the Liquid State* (Clarendon Press, Oxford, 1994).
[3] T. Scopigno, U. Balucani, G. Ruocco, and F. Sette, Phys. Rev. E **63**, 011210 (2000).
[4] T. Bryk and I. Mryglod, Phys. Rev. E **63**, 051202 (2001).
[5] W.-C. Pilgrim and C. Morkel, J. Phys.: Condens. Matter **18**, R585 (2006).
[6] L. Calderín, D. J. González, L. E. González, and J. M. López, J. Chem. Phys. **129**, 194506 (2008).
[7] S. Sengül, D. J. González, and L. E. González, J. Phys.: Condens. Matter **21**, 115106 (2009).
[8] J. Souto, M. M. G. Alemany, L. J. Gallego, L. E. González, and D. J. González, Phys. Rev. B **81**, 134201 (2010).
[9] B. G. del Rio and L. E. González, J. Phys.: Condens. Matter **26**, 465102 (2014).
[10] T. Bryk, I. Mryglod, T. Scopigno, G. Ruocco, F. Gorelli, M. Santoro, T. Bryk, I. Mryglod, T. Scopigno, and G. Ruocco, J. Chem. Phys. **133**, 024502 (2010).

[11]U. Bafile, E. Guarini, and F. Barocchi, Phys. Rev. E **73**, 061203 (2006).
[12]W. Götze, J. Phys.: Condens. Matter **1**, 873 (1998).
[13]Y. Katayama, T. Mizutani, W. Utsumi, O. Shimomura, M. Yamakata, and K. Funakoshi, Nature **403**, 170 (2000).
[14]C. Sanloup, F. Guyot, P. Gillet, G. Fiquet, R. J. Hemley, M. Mezouar, and I. Martinez, Europhys. Lett. **52**, 151 (2000).
[15]H. Reichert, O. Klein, H. Dosch, M. Denk, V. Honkimäki, T. Lippmann, and G. Reiter, Nature **408**, 839 (2000).
[16]A. Di Cicco, A. Trapananti, S. Faggioni, and A. Filipponi, Phys. Rev. Lett. **91**, 135505 (2003).
[17]S. Hosokawa, M. Inui, Y. Kajihara, K. Matsuda, T. Ichitsubo, W.-C. Pilgrim, H. Sinn, L. E. González, D. J. González, S. Tsutsui, and A. Q. R. Baron, Phys. Rev. Lett. **102**, 105502 (2009).
[18]S. Hosokawa, S. Munejiri, M. Inui, Y. Kajihara, W. C. Pilgrim, Y. Ohmasa, S. Tsutsui, A. Q. R. Baron, F. Shimojo, and K. Hoshino, J. Phys.: Condens. Matter **25**, 112101 (2013).
[19]S. Hosokawa, M. Inui, Y. Kajihara, S. Tsutsui, and A. Q. R. Baron, J. Phys.: Condens. Matter **27**, 194104 (2015).
[20]T. Bryk, G. Ruocco, T. Scopigno, and A. P. Seitsonen, J. Chem. Phys. **143**, 104502 (2015).
[21]M. Marqués, L. E. González, and D. J. González, J. Phys.: Condens. Matter **28**, 075101 (2016).
[22]M. Marqués, D. J. González, and L. E. González, Phys. Rev. B **94**, 024204 (2016).
[23]B. G. del Rio, L. E. González, and D. J. González, J. Chem. Phys. **146**, 034501 (2017).
[24]B. G. del Rio and L. E. González, Phys. Rev. B **95**, 224201 (2017).
[25]P. Hohenberg and W. Kohn, Phys. Rev. **136**, B864 (1964).
[26]Y. A. Wang and E. A. Carter, in *Theoretical Methods in Condensed Phase Chemistry*, edited by S. D. Schwartz (Springer, Dordrecht, 2002), pp. 117–184.
[27]T. A. Wesolowski and Y. A. Wang, *Recent Progress in Orbital-Free Density Functional Theory* (World Scientific, Singapore, 2013).
[28]V. V. Karasiev, D. Chakraborty, and S. B. Trickey, in *Many-Electron Approaches Physics, Chemistry, and Mathematics*, edited by V. Bach and L. Delle Site (Springer, Cham, Switzerland, 2014), pp. 113–134.
[29]L. Sjögren and A. Sjölander, J. Phys. C: Solid State Phys. **12**, 4369 (1979).
[30]L. Sjögren, Phys. Rev. A **22**, 2866 (1980).
[31]L. Sjögren, Phys. Rev. A **22**, 2883 (1980).
[32]L. Sjögren, J. Phys. C: Solid State Phys. **13**, 705 (1980).
[33]W. Kohn and L. J. Sham, Phys. Rev. **140**, A1133 (1965).
[34]B. Zhou, Y. A. Wang, and E. A. Carter, Phys. Rev. B **69**, 125109 (2004).
[35]C. Huang and E. A. Carter, Phys. Chem. Chem. Phys. **10**, 7109 (2008).
[36]M. Chen, L. Hung, C. Huang, J. Xia, and E. A. Carter, Mol. Phys. **111**, 3448 (2013).
[37]G. S. Ho, V. L. Lignères, and E. A. Carter, Comput. Phys. Commun. **179**, 839 (2008).
[38]L. Hung, C. Huang, I. Shin, G. S. Ho, V. L. Lignères, and E. A. Carter, Comput. Phys. Commun. **181**, 2208 (2010).
[39]M. Chen, J. Xia, C. Huang, J. M. Dieterich, L. Hung, I. Shin, and E. A. Carter, Comput. Phys. Commun. **190**, 228 (2014).
[40]E. Smargiassi and P. A. Madden, Phys. Rev. B **49**, 5220 (1994).
[41]D. M. Ceperley and B. J. Alder, Phys. Rev. Lett. **45**, 566 (1980).
[42]J. P. Perdew and A. Zunger, Phys. Rev. B **23**, 5048 (1981).
[43]M. Parrinello and A. Rahman, Phys. Rev. Lett. **45**, 1196 (1980).
[44]S. Nosé, J. Chem. Phys. **81**, 511 (1984).
[45]W. G. Hoover, Phys. Rev. A **31**, 1695 (1985).
[46]M. P. Allen and D. J. Tildesley, *Computer Simulation of Liquids* (Oxford University Press, 1987).
[47]T. Scopigno, U. Balucani, G. Ruocco, and F. Sette, Phys. Rev. Lett. **85**, 4 (2000).
[48]M. H. Ernst, E. H. Hauge, and J. M. J. Van Leeuwen, Phys. Rev. A **4**, 2055 (1971).
[49]M. H. Ernst, E. H. Hauge, and J. M. J. van Leeuwen, J. Stat. Phys. **15**, 7 (1976).
[50]M. H. Ernst and J. R. Dorfman, Physica **61**, 157 (1972).
[51]M. H. Ernst and J. R. Dorfman, J. Stat. Phys. **12**, 311 (1975).
[52]G. Wahnström and L. Sjögren, J. Phys. C: Solid State Phys. **15**, 401 (1982).
[53]D. Levesque and L. Verlet, Phys. Rev. A **2**, 2514 (1970).
[54]U. Balucani, R. Vallauri, T. Gaskell, and S. F. Duffy, J. Phys.: Condens. Matter **2**, 5015 (1990).
[55]W. Gudowski, M. Dzugutov, and K.-E. Larsson, Phys. Rev. E **47**, 1693 (1993).
[56]F. Shimojo, K. Hoshino, and M. Watabe, J. Phys. Soc. Jpn. **63**, 1821 (1994).
[57]U. Balucani, A. Torcini, A. Stang, and C. Morke, Phys. Scr. **T57**, 13 (1995).
[58]M. Canales and J. À. Padró, J. Phys.: Condens. Matter **9**, 11009 (1997).
[59]J. Casas, D. J. González, and L. E. González, Phys. Rev. B **60**, 10094 (1999).
[60]J. Casas, D. J. González, L. E. González, M. M. G. Alemany, and L. J. Gallego, Phys. Rev. B **62**, 12095 (2000).
[61]M. Canales and J. À. Padró, Phys. Rev. E **63**, 011207 (2000).
[62]K. Hoshino, F. Shimojo, and S. Munejiri, J. Phys. Soc. Jpn. **71**, 119 (2002).
[63]B. Schmid and W. Schirmacher, J. Phys.: Condens. Matter **23**, 254211 (2011).
[64]T. Gaskell and S. Miller, J. Phys. C: Solid State Phys. **11**, 3749 (1978).
[65]T. Gaskell and S. Miller, J. Phys. C: Solid State Phys. **11**, 4839 (1978).
[66]R. Zwanzig, J. Chem. Phys. **33**, 1338 (1960).
[67]R. Zwanzig, Phys. Rev. **124**, 983 (1961).
[68]H. Mori, Prog. Theor. Phys. **33**, 423 (1965).